

Article

Hot Working of an Fe-25Al-1.5Ta Alloy Produced by Laser Powder Bed Fusion

Aliakbar Emdadi ^{1,*} , Sebastian Bolz ² and Sabine Weiß ¹ 

¹ Department of Physical Metallurgy and Materials Technology, Brandenburg University of Technology Cottbus-Senftenberg, Konrad-Wachsmann-Allee 17, 03046 Cottbus, Germany; weiss@b-tu.de

² Department of Hybrid Manufacturing, Brandenburg University of Technology Cottbus-Senftenberg, Konrad-Wachsmann-Allee 17, 03046 Cottbus, Germany; bolzseba@b-tu.de

* Correspondence: emdadi@b-tu.de; Tel.: +49-(0)-355-69-2970

Abstract: In the present work, hot working was used as a post-processing method for Fe-25Al-1.5Ta (at.%) alloy built using laser powder bed fusion (LPBF) to refine the undesirable columnar microstructure with heterogeneous grain sizes and strong textures in the build direction. The hot deformation behavior and workability were investigated using constitutive modeling and the concept of processing maps. Uniaxial compression tests were conducted up to a true strain of 0.8 at 900 °C, 1000 °C, and 1100 °C with strain rates of 0.0013 s⁻¹, 0.01 s⁻¹, and 0.1 s⁻¹. The constitutive equations were derived to describe the flow stress–strain behavior in relation to the Zener–Hollomon parameter. Processing maps based on a dynamic materials model were plotted to evaluate the hot workability and to determine the optimal processing window as well as the active deformation mechanisms. The microstructure of the deformed specimens was characterized by scanning electron microscopy equipped with an electron backscatter diffraction detector. The results indicated a high degree of hot workability of the LPBF builds without flow instabilities over the entire deformation range tested. The epitaxially elongated grains of the as-built alloys were significantly refined after deformation through dynamic softening processes, and the porosity was reduced due to compressive deformation. The current study revealed a well-suited parameter range of 1000–1080 °C/0.004–0.012 s⁻¹ for the safe and efficient deformation of the LPBF-fabricated Fe-25Al-1.5Ta alloys. The effectiveness of the process combination of LPBF with subsequent hot forming could be verified with regard to microstructure refinement and porosity reduction.



Citation: Emdadi, A.; Bolz, S.; Weiß, S. Hot Working of an Fe-25Al-1.5Ta Alloy Produced by Laser Powder Bed Fusion. *Crystals* **2023**, *13*, 1335.

<https://doi.org/10.3390/cryst13091335>

Academic Editor: Hongbin Bei

Received: 26 July 2023

Revised: 15 August 2023

Accepted: 22 August 2023

Published: 31 August 2023



Copyright: © 2023 by the authors. Licensee MDPI, Basel, Switzerland. This article is an open access article distributed under the terms and conditions of the Creative Commons Attribution (CC BY) license (<https://creativecommons.org/licenses/by/4.0/>).

Keywords: iron aluminide; laser powder bed fusion; post-processing thermomechanical treatment; hot deformation; dynamic restoration; processing maps

1. Introduction

Hot working is one of the post-processing methods for additively manufactured metallic parts, which can reduce the solidification and processing defects and adjust the desired microstructure to improve their mechanical performance [1]. Hot working also enables the processing of shaped preforms produced by additive manufacturing (AM). The process combination of AM and hot working allows the advantages of AM and traditional forming methods to be utilized, whereby AM can be used to prepare shaped preforms that are subsequently forged into the final products [2,3]. This combination shortens the conventional multi-step forging processes for critical components, reduces tooling and processing costs, and simultaneously improves the mechanical properties of the AM material. Pruncu et al. [4] investigated the effect of hot forging on the laser powder bed fusion (LPBF) fabricated stainless steel preforms. They found that hot forging removed defects from the LPBF material, enhanced mechanical strength and ductility, and reduced anisotropy. Sizova et al. [5] proposed that hot working is an alternative to hot isostatic pressing (HIP) for the series production of LPBF-built titanium aluminides. Refinement of the microstructure occurred during hot working, whereas coarsening was

observed during HIP. Bambach et al. [6] studied the hot deformation behavior of Ti-6Al-4V samples produced by LPBF and direct energy deposition (DED). They found that both LPBF and DED builds had lower activation energies for hot deformation, lower peak flow stresses, and faster globularization rates than conventional wrought materials. Another study showed that the IN718 superalloy produced via laser metal deposition (LMD) and subsequently heat-treated exhibited similar flow stress levels compared to the conventional wrought alloy; however, hardening and recrystallization behaviors were different [7]. Hybrid manufacturing of Ti-6Al-4V components used wire arc additive manufacturing (WAAM) to fabricate a pre-shaped semi-finished part that was subsequently forged into a gas turbine blade in a single step [3]. The WAAM and hot forged blade showed the typical microstructure of the conventionally processed Ti-6Al-4V alloys and achieved tensile properties exceeding those of the cast and forged material. The Ti-6Al-4V preforms made via selective laser melting (SLM) revealed a high degree of hot workability and microstructure refinement during hot deformation [8]. In another study, a significant void closure occurred during hot compression of Ti-6Al-4V preforms made via electron beam melting (EBM) [9]. Maurya et al. [10] used processing maps to evaluate the hot deformation behavior and to optimize the parameters of the hybrid manufacturing process combining forging and WAAM for Ti-6Al-4V. Liu et al. [11] found that the DED-fabricated 316L stainless steel was subject to grain refinement during deformation at 1000 °C in a different way to the conventional wrought-annealed samples. Another study reported an alteration of the strong solidification texture of the LPBF-built 316L stainless steel during hot deformation using dynamic restoration mechanisms [12]. Zhou et al. [13] reported a higher resistance to deformation for the as-WAAM 2219 Al samples than the cast and forged samples when the deformation temperature was lower than 350 °C. Hot deformation was also revealed to be beneficial for LPBF-fabricated 18Ni-300 maraging steel concerning grain refinement [14]. Post-fabrication thermomechanical processing of additively manufactured metals and structure and property evolution was recently reviewed in [15].

Advanced iron aluminides strengthened with precipitates of the Laves phase based on C14-(Fe, Al)₂Ta exhibit excellent creep and oxidation resistance up to 800 °C [16]. They seem to be promising replacements for high-alloyed steels up to intermediate service temperatures of 650–800 °C. In a previous study by the author, the hot workability of an Fe-25Al-1.5Ta (at.%) alloy made via centrifugal investment casting was studied using the concept of processing maps at temperatures from 900 °C to 1100 °C [17]. Dynamic recovery (DRV) and dynamic recrystallization (DRX) were found to be the major flow softening mechanisms during the hot deformation of the studied alloy. The processing map revealed an optimal processing window at 910–1060 °C/0.0013–0.005 s⁻¹ with an efficiency of the power dissipation (η) of 50% and strain rate sensitivity (m) of 0.33. In addition, the results show a stable flow behavior without flow instabilities over the entire tested deformation range, indicating the high hot workability of the studied alloy. In other studies, spark plasma sintering (SPS) was used to produce an Fe-25Al-1.5Ta (at.%) alloy, and the hot deformation and recrystallization behaviors were investigated in the temperature range of 900–1100 °C [18]. The SPSed alloy with a fine-grained and equiaxed microstructure showed a high degree of hot deformability without flow instability over the whole tested deformation range. Within the optimum processing window, the SPS material underwent DRX with η between 40 and 50%. When deformed at lower temperatures of 800–850 °C, the processing map predicted a domain of flow instability at 800 °C/1 s⁻¹, due to cracking. The flow stress behavior and microstructure evolution of Fe-Al-Ta alloys fabricated by AM have been studied only to a limited degree. Preliminary investigations showed that the epitaxially elongated grains were refined during hot working of the LPBF builds made of an Fe-25Al-1.5Ta (at.%) alloy, and porosity was reduced [19,20]. Recrystallization of the as-LPBF microstructure occurred during the hot deformation in a similar way to the as-cast samples, yet with different work-hardening behaviors [21].

In order to successfully use a hybrid processing approach of AM and hot forming for advanced iron aluminides based on Fe-Al-Ta, comprehensive investigations are required to

explore the behavior of the alloys, including the flow behavior, the dynamic restoration processes, hot workability, and the microstructure evolution at elevated temperatures. Likewise, the optimal deformation window should be identified in order to run the process safely and with maximum efficiency of energy dissipation to achieve the highest degree of hot workability. Such information is not widely available in the literature for Fe-Al-Ta alloys made using AM. Therefore, the aim of the current study is to investigate the high-temperature flow stress–strain behavior and the dynamic restoration processes of an Fe-25Al-1.5Ta (at.%) alloy produced via LPBF from pre-alloyed powder material. Uniaxial compression tests are conducted up to a true strain of 0.8 at different temperatures ranging from 900 °C to 1100 °C and with strain rates from 0.0013 s^{−1} to 0.1 s^{−1}. The constitutive relations are derived to describe the flow stress behavior concerning the Zener–Hollomon (Z) parameter. Hot workability is evaluated using processing maps based on a dynamic materials model, and the safe and unsafe processing domains will be determined.

2. Materials and Methods

2.1. Specimen Manufacturing

Ingots of Fe-25Al-1.5Ta (at.%) alloy were cast and gas atomized into powder material by NANOVAL GmbH & Co. KG, Berlin, Germany. The powder batch had a fraction of +10/−45 μm and an average particle size of $d_{50} = 22.6$ μm. The concentration of the constituting elements was measured on several powder particles using energy-dispersive X-ray spectroscopy (EDX). The results gave an average content of 23.54 ± 3.30 at.% for Al, 74.77 ± 3.52 at.% for Fe, and 1.67 ± 0.42 at.% for Ta. The powder particles comprised Fe-Al matrix grains decorated by Ta-rich Laves phase precipitations. The grains were almost equiaxed in shape, with an average size of 4.5 μm, and showed no preferred crystallographic orientation.

The LPBF operations were conducted on a 400 W AconityMIDI (Aconity3D GmbH, Technology Park Herzogenrath, Aachen, Germany) under Ar atmosphere. The samples were built on a stainless steel build plate using a 67°-rotation scanning strategy with a laser power between 200 and 300 W, a scanning speed from 500 to 1500 mm/s, a layer thickness of 50 μm, and a hatching distance of 90 μm. Porosity was quantified on the surface of the polished specimens via image analysis using a digital microscope (Keyence VHX-7000, Osaka, Japan). The analysis showed that the porosity volume of the as-built samples depended on the process parameters and showed a minimum amount of approximately 1–2% for the specimens produced using a laser power of 250 W and a scanning speed of 1000 mm/s. Details on the initial powder characterization, the LPBF operations, the selection of the process parameters, and porosity formation are given in [19].

2.2. Hot Compression Tests

Isothermal compression tests were conducted under Ar-atmosphere on a lab-scale deformation dilatometer (DIL805A/D/T, TA Instruments, New Castle, DE, USA). The cylindrical specimens of $\varnothing 5 \times 8$ mm were heated to the deformation temperature at a rate of 10 K/s, and the temperature was homogenized within the specimens prior to compression testing by isothermal keeping for 3 min. The samples were deformed at temperatures between 900 °C and 1100 °C, with strain rates from 0.0013 s^{−1} to 0.1 s^{−1} up to a true strain of 0.8 followed by immediate cooling. The compression axis (CA) was perpendicular to the building direction (BD). The compression tests were performed twice for each deformation condition.

2.3. Microstructure Characterization

Metallographic investigations were performed on LPBF and deformed specimens sectioned parallel to CA. The microstructure characterization was operated on scanning electron microscopy (SEM) TESCAN AMBER (Brno, Czech Republic), equipped with an energy-dispersive X-ray spectrometer and a high-resolution electron backscatter diffraction (AZtec EBSD system, Oxford Instruments, Abingdon, UK) detector. High-angular resolu-

tion EBSD data were recorded with 2.21 μm step size and analyzed using the AZtecCrystal software (AZtec 4.3, Oxford Instruments AZtec system, Abingdon, UK). Inverse pole figure (IPF) maps parallel to the BD were calculated to study the crystallographic orientations of the LPBF builds. All observations were carried out in the center of the deformed samples.

Low- and high-angle grain boundaries (LAGBs/HAGBs) were identified by misorientations (θ) of 2–15° and more than 15°, respectively. Grain reference orientation deviation (GROD) axis maps were used to visualize substructures within the deformed grains. Grain orientation spread (GOS) was used as a metric to distinguish recrystallized grains from non-recrystallized parent grains in the EBSD microstructures [22]. The GOS shows the (mean) average value of the orientation spread for each grain. In the present study, the grains with a GOS $\leq 2^\circ$ were considered recrystallized, and those with a GOS $> 2^\circ$ were considered unrecrystallized [23].

2.4. Hot Workability Assessment

In the current study, hot workability is evaluated using the concept of processing maps [24] based on the principles of the dynamic materials model (DMM) and Ziegler flow instability criterion [25]. The details of DMM can be found in Supplementary Materials Sections S1 and S2.

3. Results

3.1. Flow Stress–Strain Behavior

Figure 1 presents the flow stress–strain curves of the LPBF-fabricated Fe-25Al-1.5Ta (at.%) samples compressed under different deformation conditions up to a true strain of 0.8. The flow stress is influenced by deformation temperature and strain rate; it increases with decreasing temperature and increasing strain rate. None of the curves shows the obvious flat shape associated with DRV. When deformed at 900 °C, a distinct initial stress peak is visible, followed by a fall in stress. The flow curves exhibit a broad stress peak for other temperatures, which falls slightly with increasing strain.

3.2. Kinetic Analysis of the Flow Behavior and the Constitutive Equations

A constitutive equation presents the functional dependence of flow stress on the hot deformation parameters, including strain, strain rate, and temperature. When a material undergoes deformation at elevated temperatures, the relationship between flow stress and processing parameters is generally expressed by the classical hyperbolic function [26]:

$$\dot{\epsilon} = A [\sinh(\alpha\sigma)]^n \exp\left(-\frac{Q}{RT}\right) \quad (1)$$

where $\dot{\epsilon}$ is the strain rate (s^{-1}), σ is the steady-state stress (MPa), Q is the apparent activation energy for the hot deformation ($\text{kJ}\cdot\text{mol}^{-1}$), T is the absolute deformation temperature (K), R is the universal gas constant ($8.314 \text{ J}\cdot\text{mol}^{-1}\cdot\text{K}^{-1}$), n is the stress component, and A and α are material constants. By taking the natural logarithm from Equation (1), Q can be obtained by:

$$Q = R \cdot \left(\frac{\partial \ln \dot{\epsilon}}{\partial \ln [\sinh(\alpha\sigma)]} \right)_T \cdot \left(\frac{\partial \ln [\sinh(\alpha\sigma)]}{\partial (1/T)} \right)_{\dot{\epsilon}} \quad (2)$$

The material constant α is provided by:

$$\alpha = \frac{\beta}{n_1} = \frac{(\partial \ln \dot{\epsilon} / \partial \sigma)_T}{(\partial \ln \dot{\epsilon} / \partial \ln \sigma)_T} \quad (3)$$

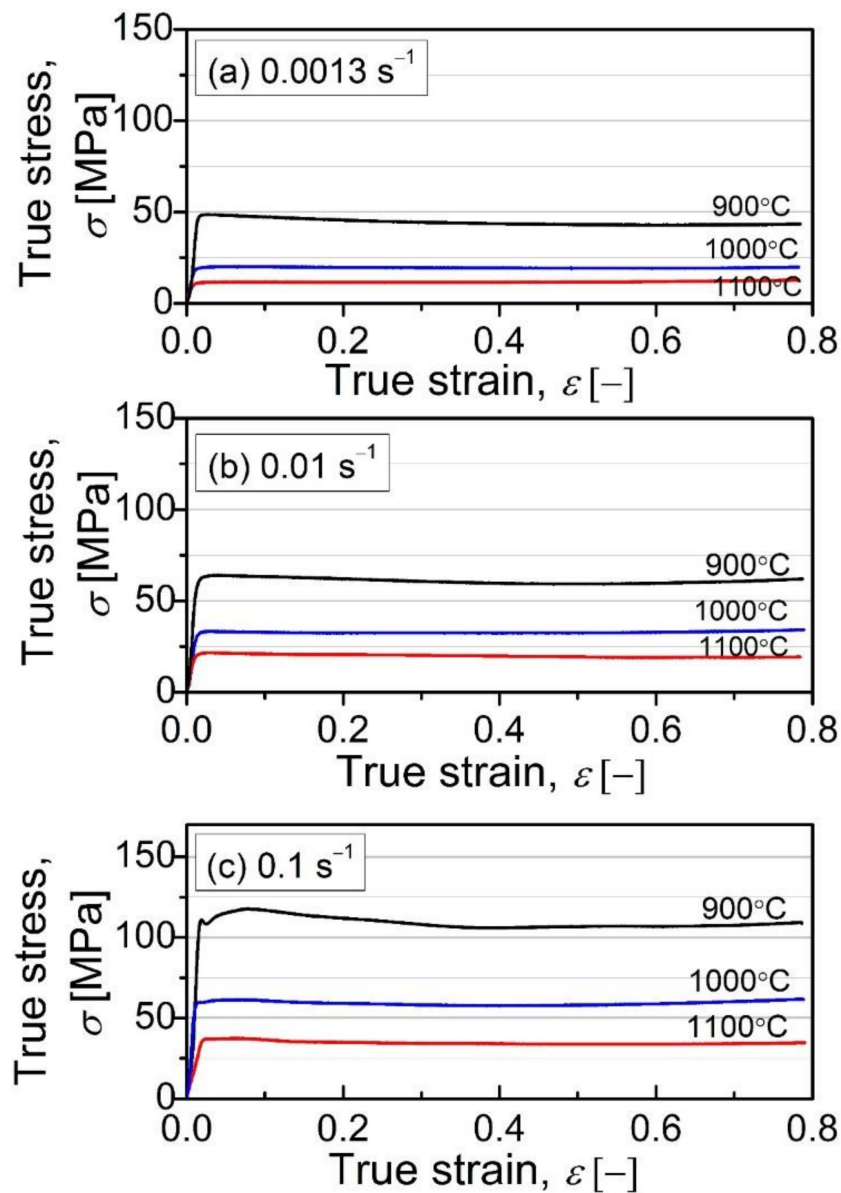


Figure 1. True stress–strain flow curves for the LPBF-fabricated Fe-25Al-1.5Ta (at.%) specimens compressed at 900 °C, 1000 °C, and 1100 °C with strain rates of 0.0013 s^{−1} (a), 0.01 s^{−1} (b), and 0.1 s^{−1} (c) up to a true strain of 0.8.

The plots for $(\ln \dot{\epsilon} - \ln \sigma)$ and $(\ln \dot{\epsilon} - \sigma)$ are plotted in Figure 2a,b. The average slope values in the plots obtained by linear regression give an average value of 4.23 for n_1 and 0.12 for β . The constant α is then calculated as 0.028 according to Equation (3). The plots for $(\ln \dot{\epsilon} - \ln[\sinh(\alpha\sigma)])$ and $(\ln[\sinh(\alpha\sigma)] - 1/T)$ at a true strain of 0.8 are plotted in Figure 2c,d. An average of 344 kJ·mol^{−1} for Q is calculated at a strain of 0.8 using the obtained slopes in the plots. The calculated Q value is comparatively lower than those values obtained for the as-cast (385 kJ·mol^{−1} [17]) and SPSeD (436 kJ·mol^{−1} [18]) Fe-25Al-1.5Ta alloys under the same deformation conditions. The lower Q for the studied LPBF alloy indicates that it has less resistance to deformation than the as-cast and the SPSeD materials.

The Zener–Hollomon parameter (Z), a temperature-compensated strain rate, is provided by:

$$Z = \dot{\epsilon} \exp\left(\frac{Q}{RT}\right) = A[\sinh(\alpha\sigma)]^n \quad (4)$$

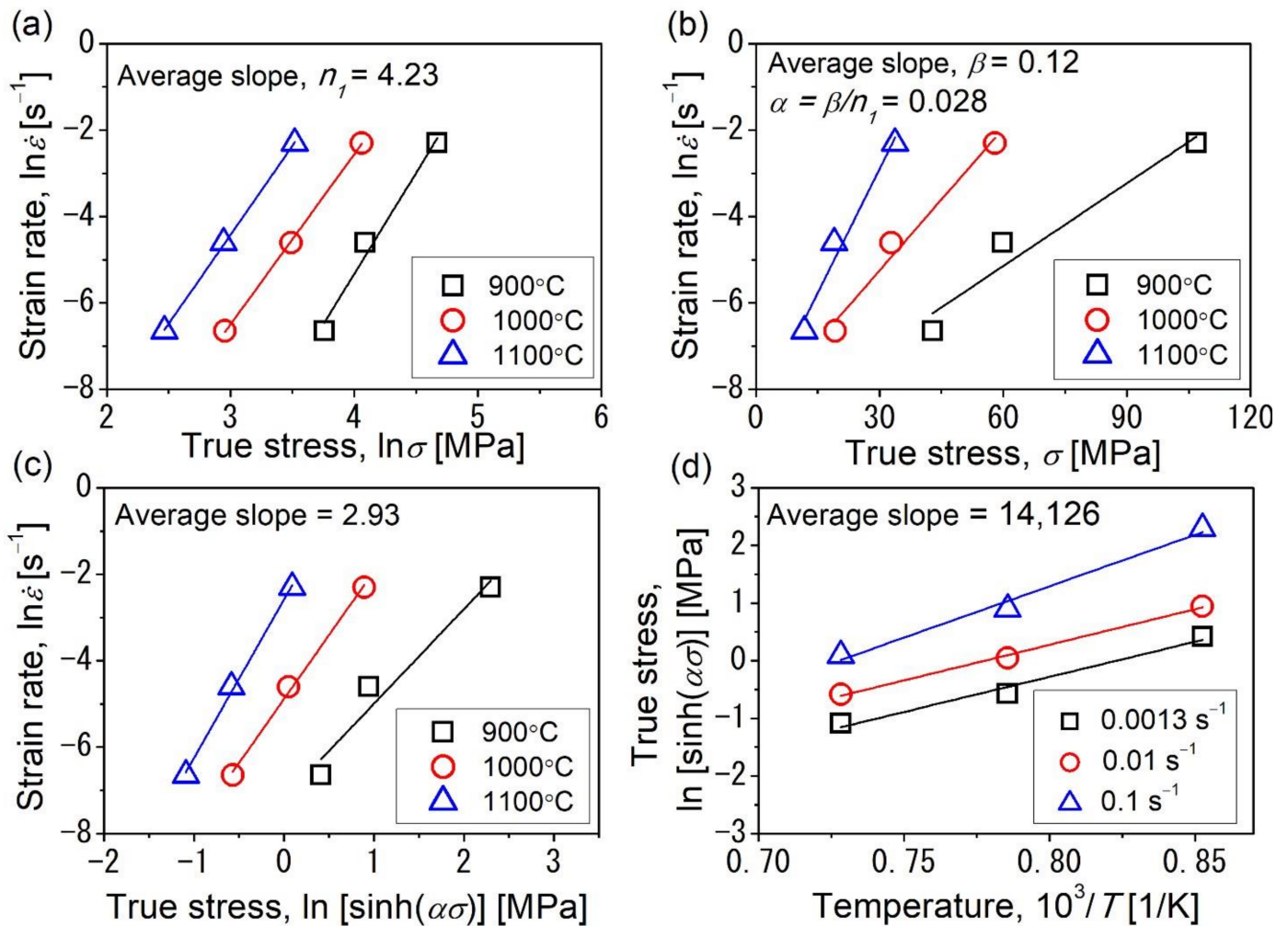


Figure 2. Kinetics analysis of the flow behavior of the LPBF Fe-25Al-1.5Ta (at.%) alloy showing linear fit for the $\ln \dot{\epsilon}$ vs. $\ln \sigma$ (a), $\ln \dot{\epsilon}$ vs. σ (b), $\ln \dot{\epsilon}$ vs. $\ln[\sinh(\alpha\sigma)]$ at different temperatures (c), and $\ln[\sinh(\alpha\sigma)]$ vs. $1/T$ at different strain rates (d) obtained from the flow curves at a strain of 0.8. The average slope values in (a) and (b) give n_1 and β , respectively, and β/n_1 gives α .

The Z values were calculated using the average Q value according to Equation (4). In Figure 3a, $\ln Z$ is plotted as a function of $\ln[\sinh(\alpha\sigma)]$ at a true strain of 0.8. The constants n and A are calculated to be 2.81 and 7.62×10^{11} using linear fitting. The constant α has already been calculated to be 0.028 using Equation (3). The constitutive equation of hot deformation in conjunction with steady-state stress can be formulated as follows:

$$\sigma = \frac{1}{0.028} \ln \left[\left(\frac{Z}{7.62 \times 10^{11}} \right)^{\frac{1}{2.81}} + \left(\left(\frac{Z}{7.62 \times 10^{11}} \right)^{\frac{2}{2.81}} + 1 \right)^{\frac{1}{2}} \right] \quad (5)$$

Figure 3b,c present the characteristic stress and strain values as a function of the dimensionless parameter Z/A [27].

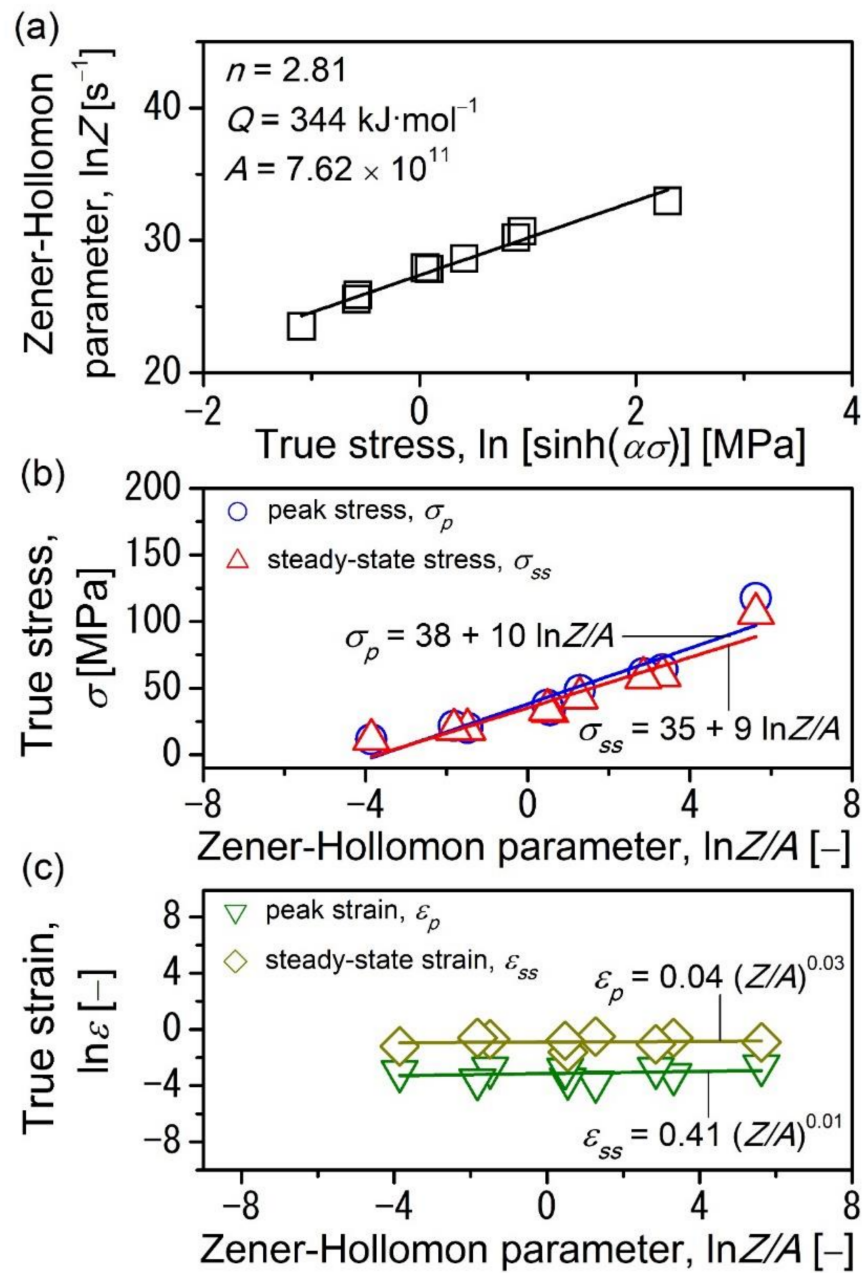


Figure 3. Relationships between $\ln Z$ and $\ln[\sinh(\alpha\sigma)]$ (a), between the dimensionless parameter Z/A and the peak stress and strain (b), and between Z/A and the steady-state stress and strain (c). The corresponding equations were derived from the linear fitting of the flow curve data at a true strain of 0.8.

4. Processing Maps

4.1. Strain Rate Sensitivity Map

A strain rate sensitivity (m , see S1 in Supplementary Materials for details) map for the studied alloy is presented in Figure 4. The m varies between 0.05 and 0.27, and regions of negative m values associated with flow instability do not appear. The highest m values occur at 1000–1100 °C/ 0.01 s^{-1} , whereas the region of the lowest m values is at 900 °C/ 0.0013 s^{-1} .

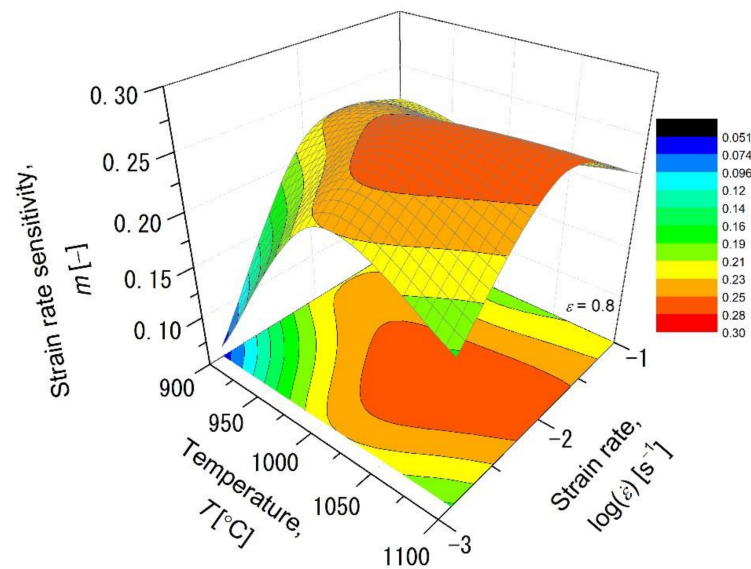


Figure 4. Three-dimensional strain rate sensitivity, m , map for the LPBF-built Fe-25Al-1.5Ta (at.%) alloy at a true strain of 0.8 showing positive m values over the entire deformation range with the highest value of 0.27 at 1000–1100 °C/0.01 s⁻¹.

4.2. Processing Map

The iso-contour processing map created at a true strain of 0.8 for the studied alloy is shown in Figure 5 (see Section S2 in Supplementary Materials for details). The numbers along the solid and dashed contours represent the efficiency of the power dissipation (η) in percent and the flow instability parameter (ζ), respectively. The map reveals no domains of negative ζ associated with flow instability over the entire deformation range investigated. The map represents a stable flow region with the highest efficiency of 43%, highlighted in yellow. The optimal processing window is situated at 1000–1080 °C/0.004–0.012 s⁻¹, with η and m of 43% and 0.27, respectively.

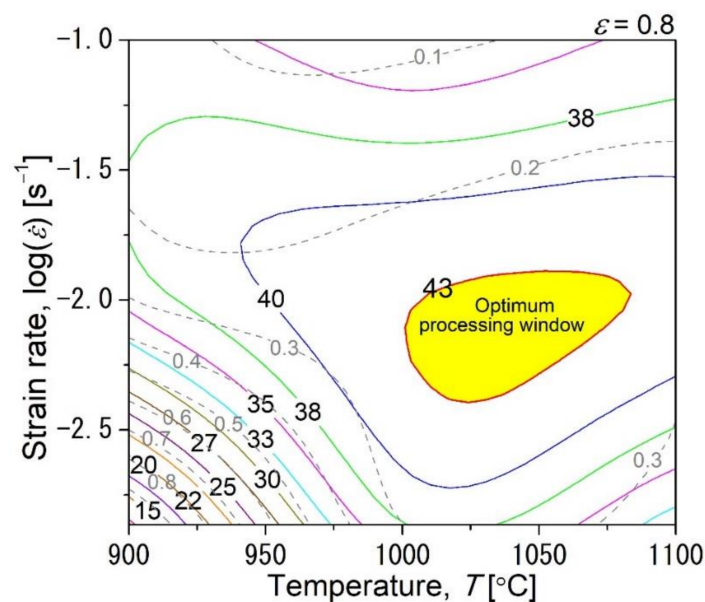


Figure 5. Processing map constructed at a true strain of 0.8 for the LPBF-built Fe-25Al-1.5Ta (at.%) alloy. The region highlighted in yellow shows the optimal processing window with the most efficient energy dissipation at 1000–1080 °C/0.004–0.012 s⁻¹. The numbers along the solid and dashed contours indicate the percent efficiency of power dissipation and the flow instability parameter, respectively.

5. Discussion

Deformation conditions significantly affect the flow stress behavior of the studied alloy at high temperatures. The flow stress declines with increasing temperature and decreasing strain rate. Evident flat shape curves associated with DRV are not observed. Nevertheless, most flow curves reveal a broad peak followed by an insignificant drop in stress. This shape is typical of the BCC α -iron, where a remarkable flow softening has not occurred in flow curves despite the occurrence of DRX [28,29]. When deformed at 900 °C, a more distinct stress peak appears.

The most efficient energy dissipation occurs in the range of 1000–1080 °C/0.004–0.012 s⁻¹, as shown by the processing map in Figure 5. The peak efficiency of 43% and the strain rate sensitivity of 0.27 suggest the occurrence of dynamic restoration processes during deformation. To investigate the microstructure evolution during hot deformation, the as-LPBF and deformed specimens were characterized by SEM and EBSD and will be discussed later.

5.1. Characterization of the As-LPBF Microstructure

Figure 6 shows the EBSD phase and the inverse pole figure (IPF) maps of the as-LPBF sample. The microstructure mainly comprises columnar grains elongated in the building direction (BD). They were extended for several millimeters across several layers along the BD. The grains exhibited a crystallographic orientation close to the $\langle 1\ 1\ 1 \rangle$ orientation with respect to the BD. Large temperature gradients and fast cooling rates during LPBF lead to the growth of elongated grains along the BD by the epitaxial growth mechanism. The as-LPBF microstructure contains approximately 44% LAGBs and 66% HAGBs. A few pores can also be seen, indicated by arrows in Figure 6a. The (Fe, Al)₂Ta C14 Laves phase precipitates occur mainly along the GBs of the matrix and occasionally within the grains; they appear blue in the phase map. It was reported that the Laves phase particles existing at the deformation temperature along the original grain boundaries in an as-cast Fe-25Al-1.5Ta alloy might act as nucleation sites during the initiation of recrystallization by a particle-stimulated nucleation (PSN) mechanism at the boundaries containing the clusters of the large particles [30]. However, the current paper does not consider the possible effects of the Laves phase precipitates on recovery and recrystallization behaviors.

5.2. Characterization of the Deformed Specimens

Figure 7a shows the SEM backscatter electron micrographs of the Fe-25Al-1.5Ta specimen compressed at 1100 °C up to a true strain of 0.8, with a strain rate of 0.01 s⁻¹. Slight deformation occurred in the dead metal zone near the forging dies. In contrast, the material underwent localized deformation in the central regions, as appears by highly deformed grains elongated perpendicular to CA. No cracks are observed, yet some pores can still be seen after deformation, mostly in the vicinity of the less-deformation and bulge zones, as pointed out by arrows in Figure 7a. In the central region of the deformed specimen, there are considerably fewer pores due to significant compressive deformation. The pores in the deformed specimens are smaller than those in the as-LPBF material, suggesting that pore closure occurred during hot deformation due to compressive stress. Figure 7b,c show high-resolution SEM images of the specimen deformed at 1100 °C/0.01 s⁻¹, taken from the bulged and central regions marked by rectangles in Figure 7a, respectively. The deformed grains are fragmented into equiaxed subregions, indicating grain refinement during hot deformation. The nature of these subregions was investigated by means of EBSD. Figure 8a shows the EBSD image quality (IQ) map overlaid with a GB misorientation map for the sample deformed at 1100 °C/0.01 s⁻¹. The deformed grains elongated perpendicular to the CA are visible. They were fragmented into subregions enclosed by low-angle boundaries, resulting from the dislocations annihilation and rearrangement into substructures (DRV) during hot deformation. The fraction of low-angle boundaries in the deformed specimen is significant (80%) compared to the as-built sample (44%), suggesting that they were further formed during deformation. These substructures can be better visualized by a grain reference orientation deviation (GROD) axis map, as shown in Figure 8b. The

average orientation is first determined for each grain. For each pixel within the grain, the misorientation axis is then calculated and displayed as a color according to the IPF color key. The GROD axis map reveals that the microstructure of the as-LPBF build has been significantly refined during deformation into substructures with different orientations.

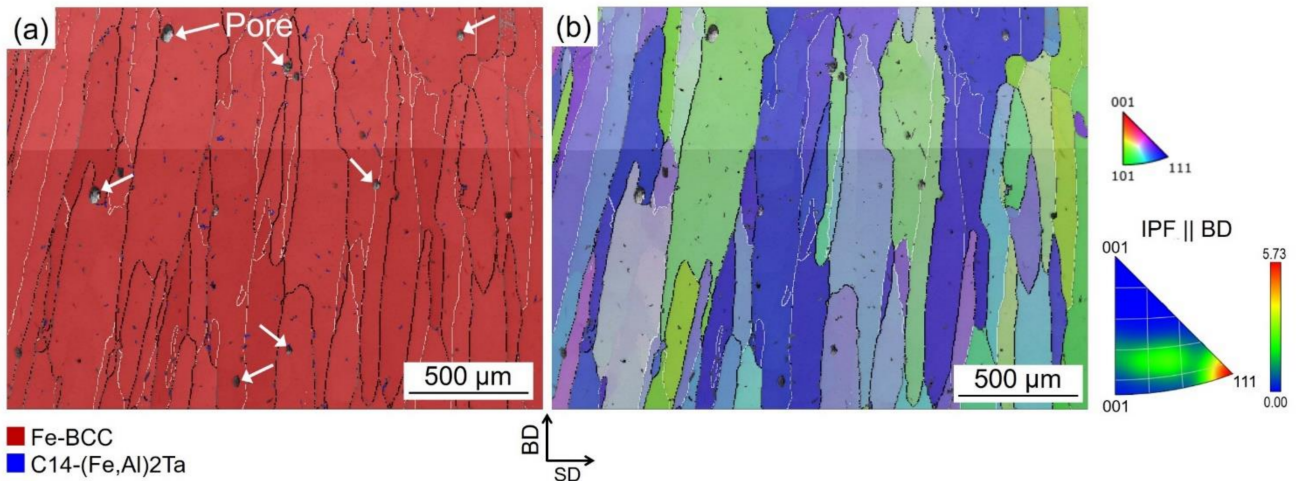


Figure 6. EBSD phase map (a) and inverse pole figure (IPF) map (b) for the as-LPBF Fe-25Al-1.5Ta (at.%) alloy showing columnar grains that are elongated in the building direction and whose crystallographic orientation is close to the $\langle 1\ 1\ 1 \rangle$ orientation. The IPF map corresponds to the orientations parallel to the BD. BD and SD refer to the build direction and the scan direction. The arrows in (a) point out some pores formed during LPBF. The C14 Laves phase precipitates appear blue on the phase map. The white and black lines correspond to low-angle grain boundaries (LAGBs) with misorientations (θ), $2^\circ \leq \theta < 15^\circ$ and high-angle grain boundaries (HAGBs) with $\theta \geq 15^\circ$, respectively. The microstructure contains approximately 44% LAGBs and 66% HAGBs. The sample was printed using a laser power of 250 W and a scanning speed of 1000 mm/s.

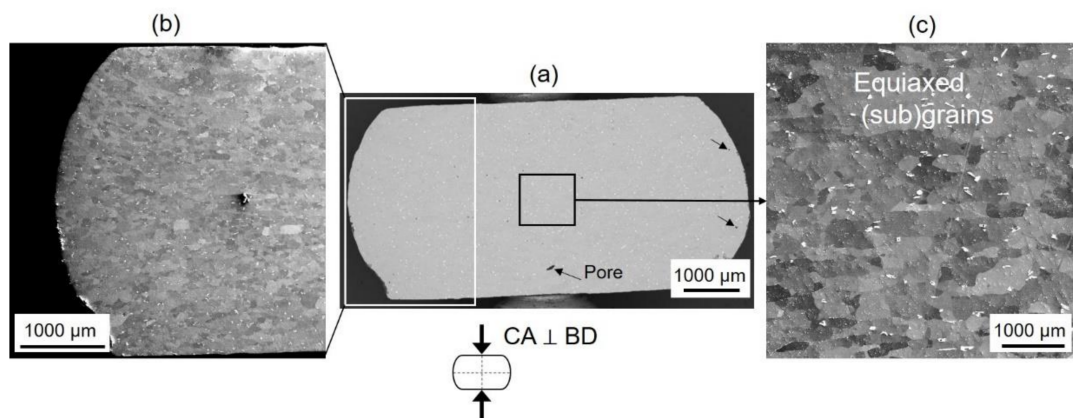


Figure 7. Representative BSE-SEM micrographs of the longitudinal cross-sections of the Fe-25Al-1.5Ta (at.%) specimen compressed at $1100^\circ\text{C}/0.01\text{ s}^{-1}/0.8$. It shows some pores marked with arrows close to the dead-metal zone and in the bulged region (a) and high-resolution images of the bulged region (b) and central region of the specimen (c) outlined by squares in (a), showing the (sub)grains within the microstructure. The Laves phase precipitates appear white in the micrographs. The specimen was compressed perpendicular to the build direction (BD). The compression axis (CA) is vertical.

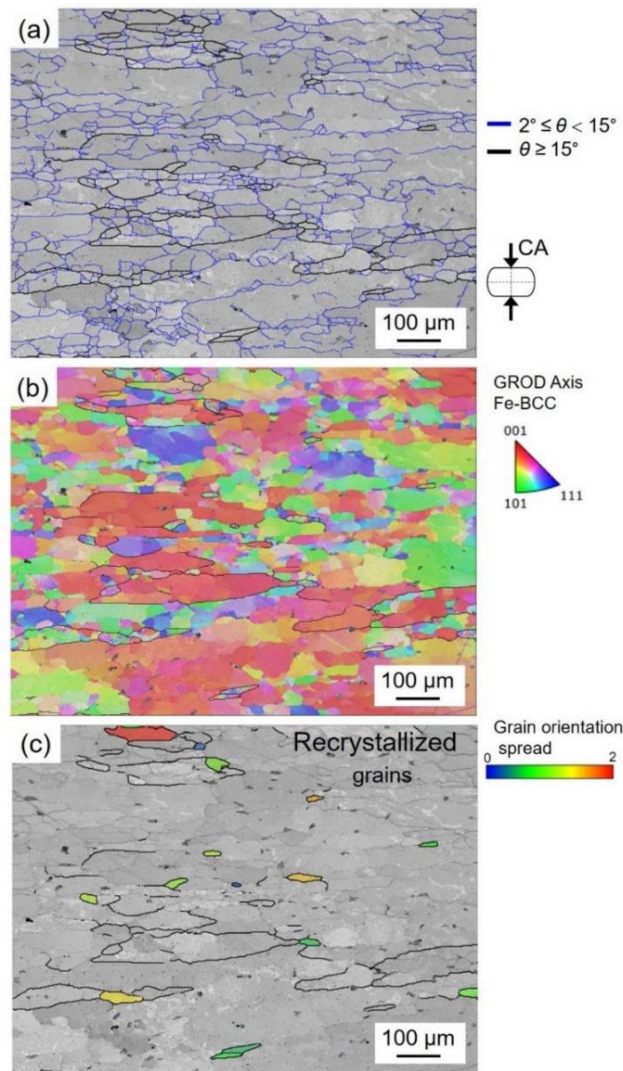


Figure 8. EBSD image quality (IQ) (a), grain reference orientation deviation (GROD)-axis (b), and grain orientation spread (GOS) (c) maps superimposed with grain boundary misorientations maps for the LPBF-fabricated Fe-25Al-1.5Ta (at.%) builds compressed at 1100 °C/0.01 s⁻¹/0.8. The blue and black lines mark low-angle grain boundaries (LAGBs) with misorientations (θ), $2^\circ \leq \theta < 15^\circ$ and high-angle grain boundaries (HAGBs) with $\theta \geq 15^\circ$, respectively. The microstructure contains approximately 80% LAGBs and 20% HAGBs. The recrystallized grains close to the grain boundary regions were separated from the un-recrystallized volume using the criterion $\text{GOS} \leq 2^\circ$ in (c). The compression axis (CA) is vertical.

Some small equiaxed grains bounded by HAGBs can also be seen adjacent to the original GBs. These small grains seem to be recrystallized grains formed likely during deformation by DRX. To verify the mechanism, grain orientation spread (GOS) was used as a metric to distinguish recrystallized grains from unrecrystallized parent grains in the EBSD microstructures. In the present study, the grains with a $\text{GOS} \leq 2^\circ$ were considered recrystallized, and those with a $\text{GOS} > 2^\circ$ were considered to be not recrystallized. Figure 8c shows that the equiaxed and fine grains near the pre-existing grain boundary regions have a GOS less than 2° , indicating that they are recrystallized grains containing less strain and, thus, misorientations inside.

5.3. Flow Softening Mechanism

Within the optimal deformation region of the processing map (1000–1080 °C/0.004–0.012 s⁻¹), a stable flow is achievable, with the highest power dissipation efficiency of 43% and a strain rate sensitivity of 0.27. The grains in the sample deformed at 1100 °C/0.01 s⁻¹/0.8 are subdivided into regions with a continuous variation of IPF colors within deformed grains in the GROD-axis map. These substructures indicate the annihilation and rearrangement of dislocations during deformation (DRV). Some substructures have already evolved into subgrains bounded with LAGBs, constituting ~80% of the boundaries, as marked by the blue lines in Figure 8a.

In addition to the substructures, small grains enclosed by HAGBs appear close to the original GBs with a GOS of less than 2°. This indicates that those grains are likely recrystallized grains containing less strain and, thus, misorientations inside. The fraction of recrystallized grains is insignificant compared to that of substructures within the deformed grains. Therefore, a combination of DRV as the primary mechanism and some DRX occurs in the samples that are deformed within the optimal processing window.

It should be mentioned that no flow instability occurred in the present study based on the Ziegler criterion of flow instability. Reliable flow behavior without instability indicates high hot workability of the LPBF-fabricated Fe-25Al-1.5Ta alloy in the 900–1100 °C/0.0013–0.1 s⁻¹ deformation range, as also reported for the as-cast and spark plasma sintered alloys [17,18].

6. Conclusions

The process combination of laser powder bed fusion with subsequent hot forming of an Fe-25Al-1.5Ta (at.%) alloy with regard to hot workability and microstructure refinement was investigated. Uniaxial compression tests were conducted up to a true strain of 0.8 in a temperature range from 900 to 1100 °C with strain rates from 0.0013 s⁻¹ to 0.1 s⁻¹. The main conclusions of the present study are summarized as follows:

The LPBF builds were characterized by columnar grains elongated across several layers along the build direction. The grains exhibited a relatively strong microtexture close to <1 1 1> with respect to the build direction.

The columnar and elongated grains of the as-built sample were remarkably refined after hot deformation, and the porosity was reduced.

The deformed specimen indicated a high degree of hot workability without flow instability.

The optimal processing window was found to be 1000–1080 °C/0.004–0.012 s⁻¹, where the alloy was subjected to a combined dynamic recovery through substructure formation and recrystallization at the original grain boundaries.

The activation energy (*Q*) for hot deformation was averaged to 344 kJ·mol⁻¹ over the studied deformation range.

The constitutive equation for hot deformation for the studied LPBF Fe-25Al-1.5Ta alloy can be formulated as:

$$\sigma = \frac{1}{0.028} \ln \left[\left(\frac{Z}{7.62 \times 10^{11}} \right)^{\frac{1}{2.81}} + \left(\left(\frac{Z}{7.62 \times 10^{11}} \right)^{\frac{2}{2.81}} + 1 \right)^{\frac{1}{2}} \right]$$

In summary, it was found that the combination of hot working with LPBF can significantly refine the microstructure of the LPBF builds and reduce their porosity. Such refined microstructure is also expected to improve the mechanical properties of the LPBF material. Therefore, hybrid routes of AM and hot forging could be a promising alternative to traditional multi-step routes for the manufacturing of difficult-to-deform engineering alloys. The advantages of AM are used to build shaped preforms that are subsequently forged into the final forged products.

Supplementary Materials: The following supporting information can be downloaded at: <https://www.mdpi.com/article/10.3390/cryst13091335/s1>, S1: Strain Rate Sensitivity Map; S2: Processing Map [31].

Author Contributions: Conceptualization, A.E. and S.W.; methodology, A.E.; investigation, A.E. and S.B.; writing—original draft preparation, A.E.; writing—review and editing, A.E. and S.W.; supervision, A.E. and S.W. All authors have read and agreed to the published version of the manuscript.

Funding: This research received no external funding.

Data Availability Statement: The data are available on request from the corresponding authors.

Acknowledgments: A. Emdadi acknowledges the Chair of Hybrid Manufacturing (FHF) at BTU Cottbus-Senftenberg for LPBF operations and compression tests.

Conflicts of Interest: The authors declare that they have no known competing financial interests or personal relationships that could have appeared to influence the work reported in this paper.

References

1. Motallebi, R.; Savaedi, Z.; Mirzadeh, H. Additive manufacturing—A review of hot deformation behavior and constitutive modeling of flow stress. *Curr. Opin. Solid State Mater. Sci.* **2022**, *26*, 100992. [[CrossRef](#)]
2. Bambach, M.; Sizova, I.; Emdadi, A. Development of a processing route for Ti-6Al-4V forgings based on preforms made by selective laser melting. *J. Manuf. Process.* **2019**, *37*, 150–158. [[CrossRef](#)]
3. Bambach, M.; Sizova, I.; Sydow, B.; Hemes, S.; Meiners, F. Hybrid manufacturing of components from Ti-6Al-4V by metal forming and wire-arc additive manufacturing. *J. Mater. Process. Technol.* **2020**, *282*, 116689. [[CrossRef](#)]
4. Pruncu, C.I.; Hopper, C.; Hooper, P.A.; Tan, Z.; Zhu, H.; Lin, J.; Jiang, J. Study of the Effects of Hot Forging on the Additively Manufactured Stainless Steel Preforms. *J. Manuf. Process.* **2020**, *57*, 668–676. [[CrossRef](#)]
5. Sizova, I.; Sviridov, A.; Bambach, M.; Eisentraut, M.; Hemes, S.; Hecht, U.; Marquardt, A.; Leyens, C. A study on hot-working as alternative post-processing method for titanium aluminides built by laser powder bed fusion and electron beam melting. *J. Mater. Process. Technol.* **2021**, *291*, 117024. [[CrossRef](#)]
6. Bambach, M.; Sizova, I.; Szyndler, J.; Bennett, J.; Hyatt, G.; Cao, J.; Papke, T.; Merklein, M. On the hot deformation behavior of Ti-6Al-4V made by additive manufacturing. *J. Mater. Process. Technol.* **2021**, *288*, 116840. [[CrossRef](#)]
7. Bambach, M.; Sizova, I.; Silze, F.; Schnick, M. Hot workability and microstructure evolution of the nickel-based superalloy Inconel 718 produced by laser metal deposition. *J. Alloys Compd.* **2018**, *740*, 278–287. [[CrossRef](#)]
8. Sizova, I.; Bambach, M. Hot workability and microstructure evolution of pre-forms for forgings produced by additive manufacturing. *J. Mater. Process. Technol.* **2018**, *256*, 154–159. [[CrossRef](#)]
9. Saboori, A.; Abdi, A.; Fatemi, S.A.; Marchese, G.; Biamino, S.; Mirzadeh, H. Hot deformation behavior and flow stress modeling of Ti-6Al-4V alloy produced via electron beam melting additive manufacturing technology in single β -phase field. *Mater. Sci. Eng. A* **2020**, *792*, 139822. [[CrossRef](#)]
10. Maurya, A.K.; Yeom, J.-T.; Kang, S.W.; Park, C.H.; Hong, J.-K.; Reddy, N.S. Optimization of hybrid manufacturing process combining forging and wire-arc additive manufactured Ti-6Al-4V through hot deformation characterization. *J. Alloys Compd.* **2022**, *894*, 162453. [[CrossRef](#)]
11. Liu, Y.; Zhang, C.; Wang, Y.; Xu, X.; Zhu, H.; Jiang, J. Reveal the hot deformation behaviour and microstructure evolution in additively manufactured 316 L stainless steel. *Mater. Sci. Eng. A* **2022**, *861*, 144290. [[CrossRef](#)]
12. Khodabakhshi, F.; Hasani, N.; Kalaie, M.R.; Hadadzadeh, A.; Wells, M.A.; Mohammadi, M. Dynamic recrystallization under hot deformation of additively manufactured 316 L stainless steel. *Mater. Charact.* **2023**, *202*, 113055. [[CrossRef](#)]
13. Zhou, Y.; Lin, X.; Kang, N.; Wang, Z.; Tan, H.; Huang, W. Hot deformation induced microstructural evolution in local-heterogeneous wire + arc additive manufactured 2219 Al alloy. *J. Alloys Compd.* **2021**, *865*, 158949. [[CrossRef](#)]
14. Tomiczek, B.; Snopiński, P.; Borek, W.; Król, M.; Gutiérrez, A.R.; Matula, G. Hot Deformation Behaviour of Additively Manufactured 18Ni-300 Maraging Steel. *Materials* **2023**, *16*, 2412. [[CrossRef](#)]
15. Shakil, S.I.; Smith, N.R.; Yoder, S.P.; Ross, B.E.; Alvarado, D.J.; Hadadzadeh, A.; Haghshenas, M. Post fabrication thermomechanical processing of additive manufactured metals: A review. *J. Manuf. Process.* **2022**, *73*, 757–790. [[CrossRef](#)]
16. Palm, M.; Stein, F.; Dehm, G. Iron Aluminides. *Annu. Rev. Mater. Res.* **2019**, *49*, 297–326. [[CrossRef](#)]
17. Emdadi, A.; Michels, H.; Tovar, M. Hot Workability Investigation of an Fe-Al-Ta Alloy Using Deformation Processing Maps. *Metals* **2023**, *13*, 1195. [[CrossRef](#)]
18. Emdadi, A.; Sizova, I.; Bambach, M.; Hecht, U. Hot deformation behavior of a spark plasma sintered Fe-25Al-1.5Ta alloy with strengthening Laves phase. *Intermetallics* **2019**, *109*, 123–134. [[CrossRef](#)]
19. Emdadi, A.; Bolz, S.; Buhl, J.; Weiß, S.; Bambach, M. Laser Powder Bed Fusion Additive Manufacturing of Fe₃Al-1.5Ta Iron Aluminide with Strengthening Laves Phase. *Metals* **2022**, *12*, 997. [[CrossRef](#)]
20. Emdadi, A.; Bolz, S.; Jensch, F.; Tovar, M.; Weiß, S. On the Hot Deformation of a Fe-Al-Ta Iron Aluminide Prepared via Laser Powder Bed Fusion. *Crystals* **2023**, *13*, 627. [[CrossRef](#)]
21. Emdadi, A.; Weiß, S. A Comparative Study of Microstructure and Hot Deformability of a Fe-Al-Ta Iron Aluminide Prepared via Additive Manufacturing and Conventional Casting. *Crystals* **2022**, *12*, 1709. [[CrossRef](#)]
22. Wagner, F.; Allain-Bonasso, N.; Berbenni, S.; Field, D.P. On the Use of EBSD to Study the Heterogeneity of Plastic Deformation. *Mater. Sci. Forum* **2011**, *702*, 245–252. [[CrossRef](#)]

23. Yan, C.K.; Feng, A.H.; Qu, S.J.; Cao, G.J.; Sun, J.L.; Shen, J.; Chen, D.L. Dynamic recrystallization of titanium: Effect of pre-activated twinning at cryogenic temperature. *Acta Mater.* **2018**, *154*, 311–324. [[CrossRef](#)]
24. Prasad, Y.V.R.K. Processing Maps: A Status Report. *J. Mater. Eng. Perform.* **2003**, *12*, 638–645. [[CrossRef](#)]
25. Narayana Murty, S.V.S.; Nageswara Rao, B. Ziegler's Criterion on the Instability Regions in Processing Maps. *J. Mater. Sci. Lett.* **1998**, *17*, 1203–1205. [[CrossRef](#)]
26. McQueen, H.J.; Ryan, N.D. Constitutive analysis in hot working. *Mater. Sci. Eng. A* **2002**, *322*, 43–63. [[CrossRef](#)]
27. Kim, S.-I.; Yoo, Y.-C. Prediction of dynamic recrystallisation behaviour of AISI type 4140 medium carbon steel. *Mater. Sci. Technol.* **2002**, *18*, 160–164. [[CrossRef](#)]
28. Tsuji, N.; Matsubara, Y.; Saito, Y. Dynamic recrystallization of ferrite in interstitial free steel. *Scr. Mater.* **1997**, *37*, 477–484. [[CrossRef](#)]
29. Tsuji, N.; Matsubara, Y.; Saito, Y.; Maki, T. Occurrence of Dynamic Recrystallization in Ferritic Iron. *J. Jpn. Inst. Met.* **1998**, *62*, 967–976. [[CrossRef](#)]
30. Emdadi, A.; Yang, Y.; Bolz, S.; Stryzhyboroda, O.; Tovar, M.; Gein, S.; Hecht, U.; Weiß, S. Mechanisms of necklace recrystallization in a BCC Fe-Al-Ta alloy with strengthening Laves phase precipitates. *Scr. Mater.* **2023**, *237*, 115705. [[CrossRef](#)]
31. Ziegler, H.; Eidgenössische Technische Hochschule. *Some Extremum Principles in Irreversible Thermodynamics, with Application to Continuum Mechanics*; Swiss Federal Institute of Technology: Zürich, Switzerland, 1962.

Disclaimer/Publisher's Note: The statements, opinions and data contained in all publications are solely those of the individual author(s) and contributor(s) and not of MDPI and/or the editor(s). MDPI and/or the editor(s) disclaim responsibility for any injury to people or property resulting from any ideas, methods, instructions or products referred to in the content.